AIAA JOURNAL
Vol. 35, No. 5, May 1997

Flow Characteristics and Shear-Layer Vortex Shedding of Double Concentric Jets

R. F. Huang* and C. L. Lin†
National Taiwan Institute of Technology, Taipei 106, Taiwan, Republic of China

The characteristics of the flow structure and shear-layer vortex shedding of double concentric jets separated by a disk are studied experimentally. Average flow patterns in the prepenetration, transition, and penetration regimes are measured. In the prepenetration regime, five characteristic flow structures are identified in the shear layer evolving from the edge of the circular disk: laminar, subcritical, transitional, supercritical, and fully turbulent modes. Periodic vortices with small fluctuations shed intermittently along the subcritical shear layer. The transitional shear layer is characterized by chaotic motion. Periodic turbulent vortices shed intermittently in the supercritical shear layer. The Strouhal number of the subcritical vortex shedding increases with the increase of annulus Reynolds number. It is constant in the supercritical mode. With the increase of central jet Reynolds number, the Strouhal number increases to a maximum at a central/annular Reynolds number ratio of 0.11 and then decreases. The Taylor's integral length scale of the subcritical shear-layer vortex shedding decreases rapidly with the increase of annulus Reynolds number. It remains constant at about 0.4 disk diameters in the supercritical mode. The Reynolds stresses of the shear layer and the stagnation point are presented and discussed. At the maximum Strouhal number of shear-layer vortex shedding in the prepenetration regime, the turbulent kinetic energy attains a maximum in the shear layer and at the stagnation point.

Nomenclature

D	= diameter of circular disk, 20 mm
d	= exit diameter of central jet, 3.4 mm
f	= frequency of shear-layer vortex shedding, Hz
Lr	= axial length of recirculation zone, from center of disk to aft stagnation point
ℓ	= Taylor's integral length scale
Re_a	= Reynolds number of annular jet ($=u_a D/\nu$)
Re_c	= Reynolds number of central jet ($=u_c d/\nu$)
r	= radial coordinate, originating from center of circular disk
r_{IVC}	= radial coordinate of inner vortex center
r_{OVC}	= radial coordinate of outer vortex center
Sr	= Strouhal number of vortex shedding ($=fD/u_a$)
u	= instantaneous axial velocity
u_a	= average exit velocity of annular jet
u_c	= average exit velocity of central jet
$\bar{u}$	= mean axial velocity
$\overline{u'u'}$	= axial normal stress of turbulence
$\overline{u'v'}$	= turbulent shear stress
$\bar{v}$	= mean radial velocity
$\overline{v'v'}$	= radial normal stress of turbulence
x	= axial coordinate, originating from center of circular disk
x_{IVC}	= axial coordinate of inner vortex center
x_{OVC}	= axial coordinate of outer vortex center
ν	= kinematic viscosity of air

Introduction

THE flow structures of the double concentric jets were extensively studied by investigators[1–8] because of their industrial applications and fundamental significance in mixing and combustion processes, e.g., nonpremixed bluff-body combustors, cooling systems, and propulsion apparatus. The performance of these jets depends on the properties of the flowfield they generate. In different ranges of velocity and diameter ratios, the flowfield presents different flow patterns and dynamic behavior. Previous research has been focused on two aspects: toroidal flow structures and unsteady vortical motions.

The mean velocity and static-pressure distributions in the region close to the exit of the nozzles of double concentric jets at Reynolds numbers higher than 10^5 were measured by Chigier and Beer.[2] They found that the length of the recirculating toroidal vortex is essentially determined by the diameter of the disk and the velocity ratio. Roquemore et al.[3] introduced a laser sheet-lighting technique coupled with a fast chemically reacting system to visualize the turbulent mixing and the vortex shedding processes. The vortices shedding along the shear layer of annular flow were observed in their experiments. Li and Tankin[4] employed a similar flow visualization method together with dimensional analysis to derive a formula for estimating the recirculation length.

Schefer et al.[5] measured the velocity field of bluff-body stabilized noncombusting and combusting jets at $(Re_a, Re_c) = (1.1\times10^5, 7\times10^3)$ with a two-component laser Doppler velocimeter (LDV). The flow pattern was in the prepenetration regime. The mean, fluctuating velocity, and turbulent kinetic energy profiles up- and downstream of the recirculation bubble were presented. Schefer et al.[6] also presented velocity and turbulence profiles of LDV measurements of three typical modes at central/annular jet velocity ratios 0.84, 1.4, and 2.8.

Martins and Ghoniem[7] employed a vorticity method to simulate the unsteady flow in the double concentric jets. The numerical results were used to investigate the effects of the diameter ratio on the dynamic processes leading to vortex shedding, mixing, and strong oscillations in the system. The Strouhal number of the composite structure shedding from the wake of the bluff body was 0.135 for $D_a/D_c = 10$. In general, the Strouhal number of shedding was between 0.1 and 0.2. Huang and Lin[8] studied the flow structures in the near wake region of the double concentric jets at low annulus velocities using a smoke-wire flow visualization technique. Several characteristic flow patterns and unsteady structures were identified on the central jet/annular flow domain. The unsteady processes including the expelling and shear-layer vortex shedding were presented.

Although the toroidal structure and unsteady vortices in the flowfield of the double concentric jets were extensively investigated, the characteristics of the shear-layer vortex shedding evolving from the edge of the bluff body as well as their influences on the complex flow properties have not yet been studied. This paper reports the experimental results of the characteristics of the flow structures in the shear layer as well as their influences on the properties of the wake flow of the double concentric jets.

Received June 6, 1996; revision received Dec. 26, 1996; accepted for publication Jan. 17, 1997.

*Professor, Department of Mechanical Engineering. Member AIAA.
†Graduate Student, Department of Mechanical Engineering.

Experimental Setup

The experiments were performed with the setup shown in Fig. 1. The annular and central jets were separately supplied with two systems consisting of ring blowers, acoustical filters, pressure regulators, needle valves, particle seeding chambers, and flow conditioners. The airstreams were fed into the flow conditioning assemblies. A circular disk was placed concentrically at the exit of a cylindrical test section, which was adapted to the exit of a nozzle. The diameters of the circular disk, central jet, and cylindrical test section were 20, 3.4, and 30 mm, respectively. The blockage ratio was 0.44. The thickness of the disk was 0.5 mm. The turbulence intensities of the central jet and annular flow at $x = 0.5$ mm were less than 0.1 and 1%, respectively. The measured velocity profile across the annular exit section was uniform to within 0.7%.

The velocity field was measured with a two-component LDV. The blue and green laser beams were separated, split, and focused through an optical system. The dimensions of measuring volumes of the green and blue components were $0.075 \times 0.075 \times 0.680$ and $0.071 \times 0.071 \times 0.645$ mm, respectively. The fringe separations of green and blue components were 2.34 and 2.22 μm, respectively. The system was configured for forward scattering with a receiving angle of 10 deg off the central axis. A Bragg cell and two electronic frequency shifters were included in the system. Two counterprocessors were used to capture the frequency of the signals. The coincidence window was set to 20 μs to ensure near simultaneous measurements of the two velocity components. The magnesium oxide particles with average diameter of 1 μm were seeded into the flow to scatter the laser light. The seeding particles can respond up to 9 kHz according to Hjelmfelt and Mockros.[9] The digital outputs of the counterprocessors were fed into a data acquisition system. Each velocity data record consisted of 3000 samples, about 0.3 s long. The average sampling rate was about 10 kHz. In calculating the flow statistics, each instantaneous realization was weighted with the interarrival time, without correction of bias if the turbulence intensity was less than 15%. If the turbulence intensity was larger than 15%, the bias caused by the larger-than-average number of high-velocity particles passing through the measuring volume was corrected as suggested by McLaughlin and Tiederman.[10]

A hot-wire anemometer was used to detect the unsteady motions in the shear layer evolving from the edge of the circular disk. The hot-wire probe was made of a platinum wire, 5 μm in diameter and 1.5 mm in length. The response capability of the anemometer was estimated to be at least 4000 Hz. The output signals of the hot-wire probe were fed simultaneously to a PC-based high-speed data acquisition system and a fast Fourier transform (FFT) analyzer to extract frequency information on the traveling eddies. The accuracy of the measured shedding frequencies depends not only on the response of the hot-wire anemometer but also on the record length and sampling rate of the FFT analyzer. The uncertainty of the frequency detected is estimated to be within 1.5% in this experiment.

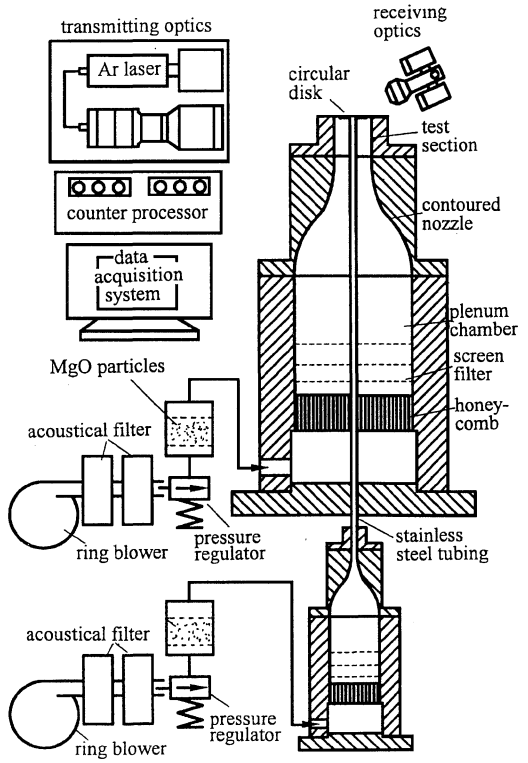

Fig. 1 Experimental setup.

Results and Discussion

Flow Characteristics

Mean Flow Patterns

Figures 2a–2d show four typical time-averaged flow patterns found in the domain of central jet/annular flow. The velocity vectors and corresponding streamline patterns are shown in the left and right halves of these figures, respectively.

The flow pattern shown in Fig. 2a is the prepenetration mode measured at $Re_a = 515$ and $Re_c = 62$. It is characterized by two stagnation points and a pair of counter-rotating vortex rings enclosed in a recirculation bubble. The separation line evolving from the edge of the disk merges to the central axis at $x/D \approx 1.35$ to form the aft stagnation point[3] (ASP), which is a four-way saddle.[11] Another four-way saddle, which is called the forward stagnation point (FSP), is formed at $x/D \approx 0.67$ in the recirculation bubble, where the central jet impinges the reverse flow. The flow branching from the FSP divides the counter-rotating vortices: the inner and outer vortices centering at the inner vortex center (IVC) and the outer vortex center (OVC), respectively. The locations of the stagnation points and size of the vortices are determined by the central jet/annular flow velocity ratio.[8] The prepenetration mode exists in the regime $Re_c/Re_a <$ 0.19–0.22 of Fig. 3.

The flow is in the transition mode while the central jet is penetrating the apex of the bubble. Although the unsteady motions of the flow are induced by the interaction of central jet and the vortical structure to overcome the maximum pressure around the apex of the bubble,[2] the time-averaged velocity field still clearly delineates the flow pattern, as shown in Fig. 2b for $Re_a = 515$ and $Re_c = 106$. Only one stagnation point is present on the apex of the bubble. Compared with those in Fig. 2a, the bubble is longer, the inner vortex is larger, and the outer vortex is smaller. The lower bound of Re_c/Re_a

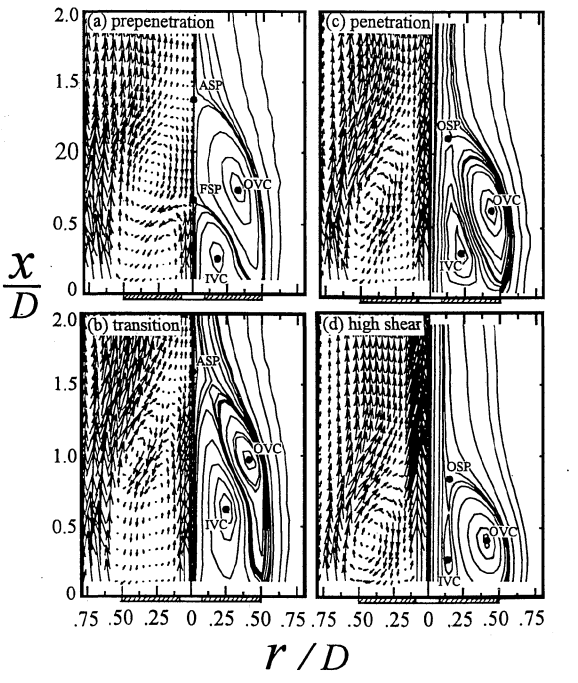

Fig. 2 Typical flow patterns (uncertainty in Re_a and $Re_c = \pm 1.5\%$): a) (Re_a, Re_c) = (515, 62); b) (Re_a, Re_c) = (515, 106); c) (Re_a, Re_c) = (515, 159); and d) (Re_a, Re_c) = (515, 536).

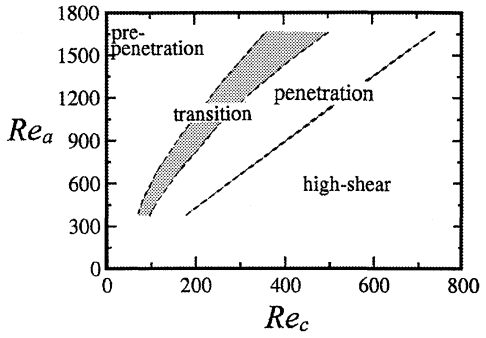

Fig. 3 Characteristic regimes of different flow patterns (uncertainty in Re_a and $Re_c = \pm 1.5\%$).

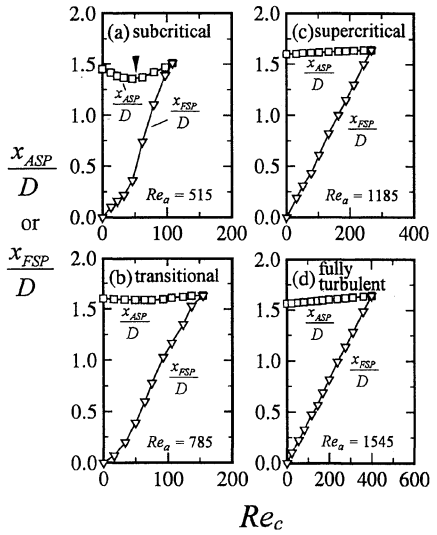

Fig. 4 Axial locations of aft and forward stagnation points (uncertainty in x_{ASP}/D and $x_{FSP}/D = \pm 0.1\%$).

of the transition region is between 0.19 and 0.22, whereas the upper bound is between 0.26 and 0.29, as shown in Fig. 3.

Figure 2c shows the flow pattern of the penetration mode measured at $Re_a = 515$ and $Re_c = 159$. The central jet penetrates the bubble so that no stagnation points are found on the central axis. An off-axis stagnation point (OSP) exists at $(x/D, r/D) \approx (1.13, 0.14)$. The penetration mode exists in the regime $Re_c/Re_a >$ 0.26–0.29 of Fig. 3. The axial length of the vortex ring shortens drastically with the increase of the central jet velocity in the regime $Re_c/Re_a < 0.43$. The inner vortex ring shrinks, and the outer vortex ring becomes wider and shorter, compared with those in Fig. 2b.

For a central jet/annular flow velocity ratio of $Re_c/Re_a > 0.43$, as shown in the high-shear regime of Fig. 3, the shortening of the axial length of the vortex ring with the increase of the central jet velocity becomes insignificant. As shown in Fig. 2d for $Re_a = 515$ and $Re_c = 536$, a large amount of annular jet fluid is entrained by the high-speed central jet because of the effect of the high shear rate. Compared with Fig. 2c, the inner vortex ring becomes very slim and the outer vortex ring appears much shorter.

Locations of Singular Points

The axial locations of ASP and FSP in the prepenetration regime are shown in Fig. 4. They are detected with LDV for points with zero average velocity on the central axis. At the low-annulus Reynolds number $Re_a = 515$ shown in Fig. 4a, the value of x_{ASP}/D decreases from about 1.5 to a minimum about 1.35 at $Re_c \approx 55$, then increases with the increase of the central-jet Reynolds number until penetration occurs. The minimum values of x_{ASP}/D are normally found at $Re_c/Re_a \approx 0.11$. The value of x_{FSP}/D increases almost linearly with the increase of central-jet Reynolds number for Re_c less than about 55. Then the slope of the curve increases considerably. The

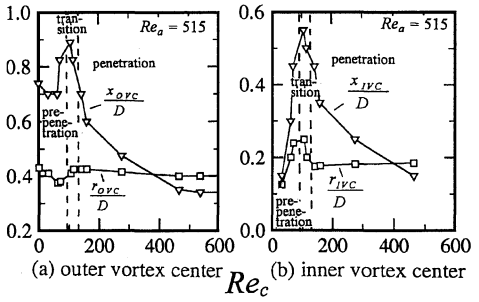

Fig. 5 Axial and radial locations of IVCs and OVCs (uncertainty in x_{OVC}/D and $r_{OVC}/D = \pm 0.1\%$).

FSP merges to the ASP as the central jet is penetrating the bubble. At an annulus Reynolds number higher than about 640, the values of x_{ASP}/D and x_{FSP}/D increase almost linearly with the increase of the central-jet Reynolds number, as shown in Figs. 4b, 4c, and 4d for $Re_a = 785$, 1185, and 1545, respectively.

The axial and radial locations of OVC and IVC at $Re_a = 515$ are shown in Figs. 5a and 5b. In Fig. 5a, the x_{OVC}/D and r_{OVC}/D have minimum values at $Re_c \approx 55$, which has the shortest recirculation length. For $Re_c/Re_a < 0.11$, the OVC moves upstream and inward with the increase of the central-jet Reynolds number, which causes the recirculation length to shorten. For $Re_c/Re_a > 0.11$, the OVC moves downstream and outward, causing the recirculation bubble to grow. Both x_{OVC}/D and r_{OVC}/D have maximum values at penetration in the transition regime. After the penetration, the OVC moves upstream with the increase of the central-jet Reynolds number. However, the radial position of OVC does not change appreciably in the penetration regime. In Fig. 5b, the values of x_{IVC}/D and r_{IVC}/D increase in the prepenetration regime, then attain the maximum values in the transition regime. After the penetration, the IVC moves upstream rapidly with the increase of central-jet Reynolds number. However, it does not move radially in the penetration regime.

In the prepenetration regime, the introduction of a small central-jet velocity into the recirculation bubble leads to a pressure drop in the recirculation bubble to satisfy the conservation law of momentum flux.[2] The recirculation toroid thus shortens and shrinks. Consequently, the OVC moves upstream and inward. With further increase of the central-jet velocity, the momentum of the central jet becomes large enough to overcome the impingement of the reverse flow so that the inner vortex enlarges, causing the enlargement of the slope of x_{FSP}/D in Fig. 4a. The outer vortex is pushed outward and upward so that the recirculation toroid enlarges. As the central-jet velocity increases, penetrating the bubble, the OVC and IVC locate at the highest and most outward positions. The bubble length attains its largest value. After the penetration, the large entrainment effect of the central jet causes shrinkage of the axial length of the vortex ring. The OVC and IVC thus rapidly move upstream without appreciable change of radial positions.

Characteristics of Shear-Layer Vortex Shedding

Characteristic Modes of Vortex Shedding

Along the separation line evolving from the disk edge, the shear layer develops. The instability waves develop in the upstream area of the shear layer, then evolve to form vortices as they travel downstream along the shear layer, and eventually break into small eddies in the downstream area of the stagnation point,[4,8] as shown in Fig. 6. The bimodal characteristic of the probability density function obtained by Schefer et al.[6] also supports the existence of vortex shedding in the shear layer. When a hot-wire probe is placed in the shear layer, five types of signals are identified in the prepenetration regime, as shown in Fig. 7. They are laminar, subcritical, transitional, supercritical, and fully turbulent modes. The shear-layer vortex shedding is intermittently found in the subcritical and supercritical regimes of the prepenetration mode, but hardly found in the transition and penetration modes.

In the regime of the laminar mode of Fig. 7, the velocity fluctuation of the hot-wire signal is relatively low. No particular periodic signal is found. In the regime of the subcritical mode of Fig. 7,

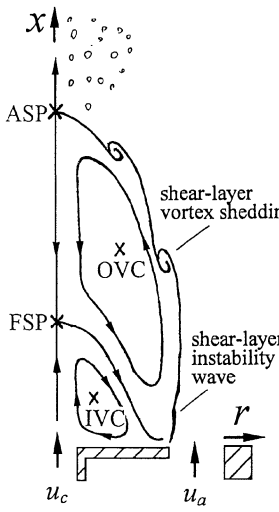

Fig. 6 Shear-layer vortex shedding evolving from disk edge.

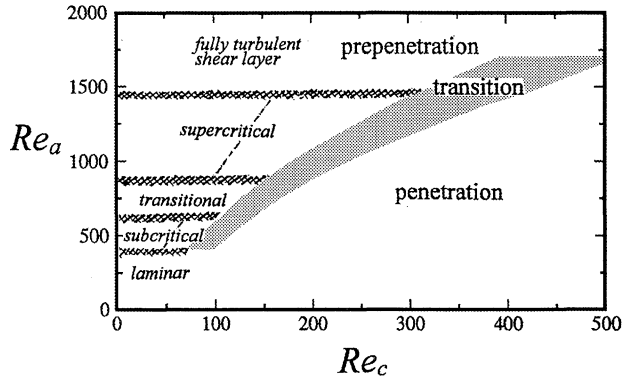

Fig. 7 Characteristic regimes of shear-layer flow modes (uncertainty in Re_a and $Re_c = \pm 1.5\%$).

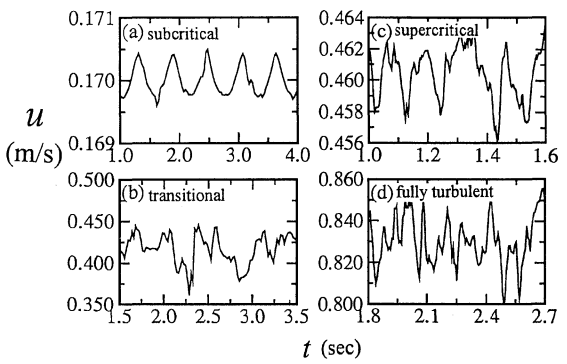

Fig. 8 Output signals of hot-wire anemometer for various characteristic flow modes of shear layer (uncertainty in $u = \pm 1.5\%$): a) $(Re_a, Re_c) = (515, 75)$, $(x/D, r/D) = (0.5, 0.725)$; b) $(Re_a, Re_c) = (785, 55)$, $(x/D, r/D) = (0.5, 0.725)$; c) $(Re_a, Re_c) = (1159, 179)$, $(x/D, r/D) = (0.51, 0.725)$; and d) $(Re_a, Re_c) = (1545, 106)$, $(x/D, r/D) = (0.515, 0.725)$.

the periodic hot-wire signals superimposed by small fluctuations, as shown in Fig. 8a, appear intermittently. The vortices shed intermittently in the shear layer. In the regime of transitional mode of Fig. 7, signals with random fluctuation appear, as shown in Fig. 8b. No particular peak is found in the power spectrum of the velocity signal. In the regime of the supercritical mode of Fig. 7, periodic hot-wire signals superimposed on large turbulent fluctuations, as shown in Fig. 8c, are present intermittently. Turbulent vortices are shed in the shear layer. In the regime of the fully turbulent mode of Fig. 7, random signals with large fluctuations are observed, as shown in Fig. 8d. The power spectrum of the velocity signal shows no particular peaks.

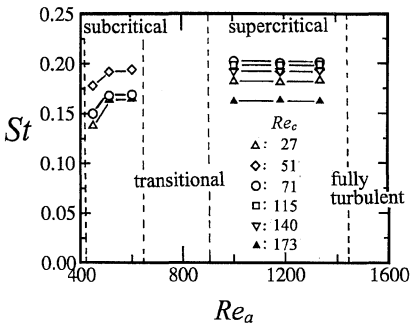

Fig. 9 Variation of Strouhal number of shear-layer vortex sheddin with annulus Reynolds number (uncertainty in $Sr = \pm 3\%$).

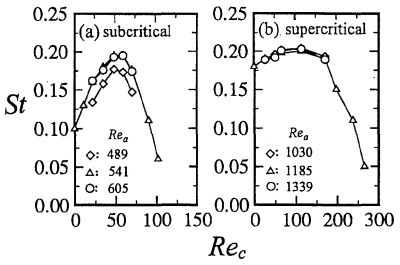

Fig. 10 Influence of central-jet Reynolds number on Strouhal numbe of shear-layer vortex shedding (uncertainty in $Sr = 3\%$).

Strouhal Number of Shear-Layer Vortex Shedding

Figure 9 shows the variation of the Strouhal number of shear-laye vortex shedding with Re_a at several central-jet Reynolds number: For each Re_c, the Strouhal number of the shear-layer vortex shec ding of the subcritical mode increases with the increase of Re_a fc $Re_a < 515$, then approaches a constant. The Strouhal numbers of th supercritical vortex shedding are constant between 0.16 and 0.2(depending on the value of Re_c.

The effects of the central jet on the Strouhal number of the shea layer vortex shedding are shown in Fig. 10. At $Re_c = 0$, the Strouh numbers are about 0.10 and 0.18 in the subcritical and supercrit cal regimes, respectively. The Strouhal number of the vortex shec ding at $Re_c = 0$ measured by Kenworthy[12] is 0.10. The numeric results of Najm and Ghoniem[13] for varieties of bluff-body cor figurations are between 0.1 and 0.2. With the introduction of th central jet, the shedding frequency increases to a maximum valu at $Re_c/Re_a \approx 0.11$, then decreases with the increase of central-je Reynolds number. The dashed lines with the slope $Re_c/Re_a \approx 0.1$ in Fig. 7 show the locus of the maximum shedding frequencies a fixed annulus Reynolds numbers.

Length Scales of Shear-Layer Vortex Shedding

To estimate the statistical size of eddies, Taylor's integral lengt scale ℓ is calculated by using the Taylor's integral timescale obtaine from the autocorrelation data and time-averaged velocity in the shea layer. The Taylor's hypothesis of a frozen flowfield is assumec The variations of the normalized Taylor's integral length scale ℓ/l with the annulus Reynolds number are shown in Fig. 11a. In th subcritical regime, ℓ/D decreases with the increase of Re_a, whera in the supercritical regime, the values of ℓ/D are smaller than thos of subcritical mode and vary inappreciably with Re_a. The Taylor' integral length scale of the supercritical vortex shedding is abou $0.4D$.

The effects of the central-jet Reynolds number on the Taylor's in tegral length scale of the shear-layer structure are shown in Fig. 11b For the subcritical and supercritical modes, ℓ/D decreases with th increase of Re_c to a minimum at $Re_c/Re_a \approx 0.11$, then increase with the increase of Re_c. In the transitional and fully turbuler regimes, ℓ/D is about 0.13 and 0.1, respectively. The central jet ha no apparent effect on the integral length scales of the shear-laye turbulence in the regimes where no vortex shedding is observec The length scales of subcritical vortices are larger than those c

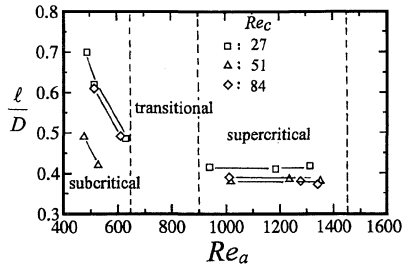

a) Variation with Re_a

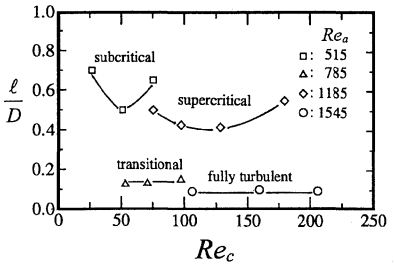

b) Variation with Re_c

Fig. 11 Taylor's integral length scale of shear-layer vortex shedding (uncertainty in $\ell/D = \pm 3\%$).

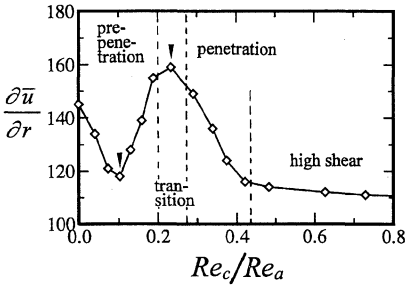

Fig. 12 Velocity gradient across shear layer (uncertainty in $\bar{u} = \pm 1.5\%$).

supercritical vortices. The length scales of the vortical structures of the subcritical and supercritical modes are much larger than those of the turbulent eddies in the transitional and fully turbulent regimes.

Velocity Gradient Across Shear Layer

The velocity gradient across the shear layer provides a measure of the growth rate and shedding frequency of the orderly structures.[14] A large velocity gradient across the mixing layer causes a large growth rate and low shedding frequency of the orderly structures in the shear layer. Figure 12 shows the velocity gradient across the shear layer. The data were measured at $Re_a = 541$ on the level $x/D = 0.73$. In the prepenetration regime, the velocity gradient across the shear layer has a minimum at $Re_c/Re_a \approx 0.11$, where the Strouhal number is a maximum and Taylor's integral length scale is a minimum. For $Re_c/Re_a < 0.11$, the introduction of the central jet to the recirculation bubble leads to the shrinkage of the bubble and outer vortex, as shown in Figs. 4a and 5a, respectively. By considering the conservation of angular momentum flux, the axial velocity in the outer vortex must increase. The velocity gradient $\partial\bar{u}/\partial r$ thus decreases with the increase of central-jet velocity. This leads to the increase of the Strouhal number and the decrease of the Taylor's integral length scale. For $Re_c/Re_a > 0.11$ in the prepenetration regime, the situations are reversed. The bubble and outer vortex enlarge and the velocity gradient increases with the increase of central-jet velocity. The velocity gradient attains a maximum in the transition regime. After the penetration of the central jet through the bubble, the bubble size shrinks rapidly in the regime $Re_c/Re_a < 0.43$ and thus the velocity gradient across the shear layer decreases considerably with the increase of Re_c. It does not change drastically as $Re_c/Re_a > 0.43$. The value of x_{OVC}/D in

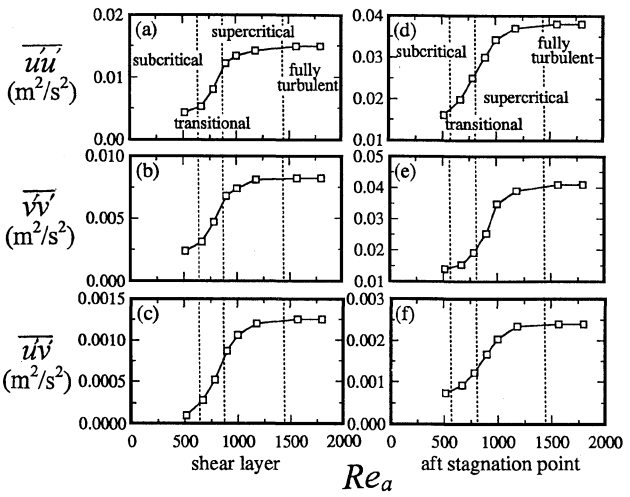

Fig. 13 Turbulence properties in shear layer and at stagnation point ($Re_c = 55$; uncertainties in $\overline{u'u'}$, $\overline{v'v'}$, and $\overline{u'v'} = \pm 3$, ± 4, and $\pm 5\%$, respectively): a), b), and c) measured at $(x/D, r/D) \approx (0.725, 0.5\text{–}0.575)$ and d), e), and f) measured at $(x/D, r/D) \approx (1.3\text{–}1.65, 0)$.

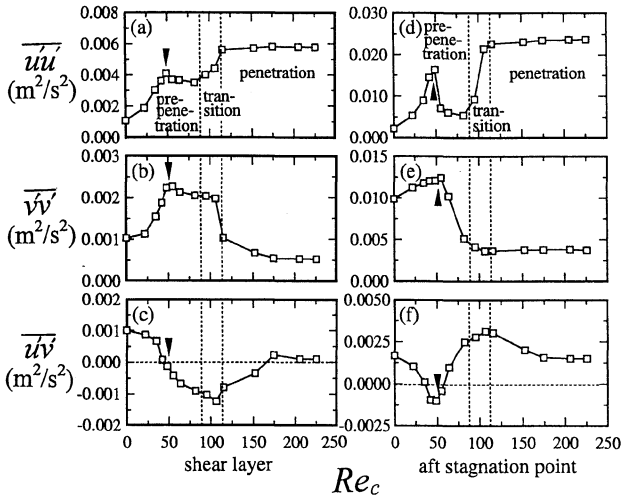

Fig. 14 Effects of central-jet velocity on the turbulence properties in shear layer and at stagnation point ($Re_a = 515$; uncertainties in $\overline{u'u'}$, $\overline{v'v'}$, and $\overline{u'v'} = \pm 3$, ± 4, and $\pm 5\%$, respectively): a), b), and c) $(x/D, r/D) \approx (0.725, 0.5\text{–}0.575)$ and d), e), and f) $(x/D, r/D) \approx (1.3\text{–}1.55, 0)$.

Fig. 5a also has this characteristic, indicating that the bubble size does not shrink significantly with the increase of central-jet velocity in the high-shear regime.

Turbulence Properties in Shear Layer and at the ASP

The Reynolds stresses measured by a two-component LDV in the shear layer and at the aft stagnation point for various characteristic modes at $Re_c = 55$ are shown in Figs. 13a–13c. Because the spatial position of shear layer changes with Reynolds number, the locations of measurements are slightly adjusted in the region $(x/D, r/D) = (0.75\text{–}0.85, 0.45\text{–}0.65)$ for different Reynolds numbers. The Reynolds stresses measured at the ASP are shown in Figs. 14d–14f. Because the axial position of the ASP changes with Reynolds number, the locations of the measurements are slightly adjusted in the region $(x/D, r/D) = (1.4\text{–}1.6, 0)$ for zero average velocities at different Reynolds numbers.

In the shear layer, the variations of the Reynolds stresses $\overline{u'u'}$, $\overline{v'v'}$, and $\overline{u'v'}$ are closely related to the characteristic flow structures of the shear layer, as shown in Figs. 13a–13c. The Reynolds stresses have low values when the coherent structures in the shear layer are in the subcritical regime. As the coherent structures are in the transitional regime, the Reynolds stresses increase significantly. In the supercritical regime, the Reynolds stresses increase slowly with annulus Reynolds number. The Reynolds stresses remain almost

constant in the fully turbulent regime. The magnitude $\overline{u'u'}$ is almost two times that of $\overline{v'v'}$. The intense vortex stretching in the axial direction may cause the value of $\overline{u'u'}$ to be larger than that of $\overline{v'v'}$. The Reynolds stresses at the ASP, as shown in Figs. 14d–14f, display patterns similar to those in the shear layer. However, the values at the stagnation point are larger than those in the shear layer, particularly the radial normal stress $\overline{v'v'}$. The energy exchange induced by the processes of turning, stretching, and impingement around the ASP generates the intense fluctuation.

Figures 14a–14c show the effects of the central-jet velocity on the Reynolds stresses in the shear layer. Figures 14d–14f show the turbulence properties at ASP (prepenetration and transition regimes) and in the penetrated jet (penetration regime). In the penetration regime, the position of measurements was not changed with Re_c. In Figs. 14a and 14b, the axial normal stresses $\overline{u'u'}$ and $\overline{v'v'}$ of the subcritical shear layer in the prepenetration regime have local maximum values at $Re_c \approx 55$, where the Strouhal number of the shear-layer vortex shedding is a maximum, as shown in Fig. 10a. The value of $\overline{u'u'}$ increases rapidly in the transition regime, then remains almost a constant in the penetration regime. However, $\overline{v'v'}$ decreases rapidly in the transition regime, then approaches a small constant value in the penetration regime. The axial normal stresses at the ASP, as shown in Figs. 14d and 14e, display the patterns similar to those in the shear layer, although the values are much higher than those in the shear layer. In the prepenetration regime, the normal stresses also peak at $Re_c \approx 55$, where the Strouhal number of the shear-layer vortex shedding maximizes. The large axial velocity of the central jet induces a high axial shear effect and generates large values of $\overline{u'u'}$ at high central-jet velocities.

The turbulent shear stress $\overline{u'v'}$ in the shear layer decreases with the increase of the central-jet velocity in the prepenetration regime, as shown in Fig. 14c. It is almost zero-valued at $Re_c \approx 55$, where the velocity gradient across the shear layer is a minimum. It has a negative maximum in the transition regime and increases in the penetration regime. At the ASP, the turbulent shear stress has a negative maximum at $Re_c \approx 55$ and a positive maximum in the transition regime.

Concluding Remarks

In the prepenetration mode of the double concentric jets, five characteristic flow structures are identified in the shear layer evolving from the edge of the circular disk: laminar, subcritical, transitional, supercritical, and fully turbulent modes. The shear layer is laminar for $Re_a < 390$. In the subcritical regime $390 < Re_a < 640$, the periodic vortices shed intermittently along the shear layer. In the transitional regime $640 < Re_a < 900$, the shear layer is characterized by chaotic motion. In the supercritical regime $900 < Re_a < 1450$, the periodic turbulent vortices shed intermittently in the shear layer. For $Re_a > 1450$, the shear layer becomes fully turbulent. The Strouhal numbers of the shear-layer vortex shedding of the subcritical mode increase with the increase of annulus velocity, then approach a constant. However, the Strouhal numbers of the supercritical vortex shedding are constant between 0.16 and 0.20. For fixed annulus velocities, the Strouhal number increases to a maximum at $Re_c/Re_a \approx 0.11$, then decreases with the increase of central-jet Reynolds number. The Taylor's integral length scales of the subcritical shear-layer vortex shedding decreases rapidly from about 0.7 to $0.4D$ with the increase of annulus Reynolds number. The length scale approaches a constant value of about $0.40D$ in the su percritical mode. In the subcritical shedding mode, the recirculatio length of the prepenetration bubble decreases with the increase o the central-jet Reynolds number to a minimum at $Re_c/Re_a \approx 0.11$ then increases to a maximum at transition.

The turbulence properties in the shear layer and at the stagnatio point are closely related to the characteristic modes of vortex shed ding. With the increase of annulus Reynolds number, the Reynold stresses are small in the subcritical mode, increase considerably i the transitional mode, increase a little in the supercritical mode, an are almost constants in the fully turbulent mode. For fixed-annulu Reynolds number in the prepenetration regime, the turbulent kineti energy attains maximum under the condition of maximum Strouha number of shear-layer vortex shedding.

References

[1]Beer, J. M., Chigier, N. A., and Lee, K. B., "Modeling of Double Con centric Burning Jets," *Ninth Symposium (International) on Combustion* Academic, New York, 1963, pp. 892–900.

[2]Chigier, N. A., and Beer, J. M., "The Flow Region Near the Nozzle i Double Concentric Jets," *Journal of Basic Engineering*, Vol. 86, Dec. 1964 pp. 797–804.

[3]Roquemore, W. M., Tankin, R. S., Chiu, H. H., and Lottes, S. A., "A Study of a Bluff-Body Combustor Using Laser Sheet Lighting," *Experiment in Fluids*, Vol. 4, No. 4, 1986, pp. 205–213.

[4]Li, X., and Tankin, R. S., "A Study of Cold and Combusting Flow Aroun Bluff Body Combustors," *Combustion Science and Technology*, Vol. 52 No. 4, 1987, pp. 173–206.

[5]Schefer, R. W., Namazian, M., and Kelly, J., "Velocity Measurements in Turbulent Nonpremixed Bluff-Body Stabilized Flame," *Combustion Scienc and Technology*, Vol. 56, Nos. 4–6, 1987, pp. 101–138.

[6]Schefer, R. W., Namazian, M., and Kelly, J., "Velocity Measurement in Turbulent Bluff-Body Stabilized Flows," *AIAA Journal*, Vol. 32, No. 9 1994, pp. 1844–1851.

[7]Martins, L.-F., and Ghonuem, A. F., "Simulation of the Nonreactin Flow in a Bluff-Body Burner; Effect of the Diameter Ratio," *Journal o Fluids Engineering*, Vol. 115, No. 3, 1993, pp. 474–484.

[8]Huang, R. F., and Lin, C. L., "Visualized Flow Patterns of Double Con centric Jets at Low Annulus Velocities," *AIAA Journal*, Vol. 32, No. 9, 1994 pp. 1868–1874.

[9]Hjelmfelt, A. T., and Mockros, L. F., "Motion of Discrete Particles i a Turbulent Fluid," *Applied Scientific Research*, Vol. 16, No. 12, 1966, pp 149–154.

[10]McLaughlin, D. K., and Tiederman, W. G., "Bias Correction fo Individual Realization of Laser Doppler Anemometer Measurements i Turbulent Flows," *Physics of Fluids*, Vol. 16, No. 12, 1973, pp. 2082-2088.

[11]Hunt, J. C. R., Abell, C. J., Peterka, J. A., and Woo, H., "Kinematica Studies of the Flows Around Free or Surface-Mounted Obstacles; Applyin Topology to Flow Visualization," *Journal of Fluid Mechanics*, Vol. 86, No. 6 1978, pp. 179–200.

[12]Kenworthy, J. S., "The Flow and Mixing in Double Concentric Jets," Ph.D. Dissertation, Dept. of Mechanical Engineering, Univ. of Sheffield England, UK, 1971.

[13]Najm, H. N., and Ghoniem, A. F., "Numerical Simulation of the Con vective Instability in a Dump Combustor," *AIAA Journal*, Vol. 29, No. 6 1991, pp. 911–919.

[14]Ho, C.-H., and Huerre, P., "Perturbed Free Shear Layers," *Annual Re view of Fluid Mechanics*, Vol. 16, 1984, pp. 365–424.

S. Gleg
Associate Editor